Journal of Nuclear Materials 402 (2010) 93–101

Contents lists available at ScienceDirect

Journal of Nuclear Materials

journal homepage: www.elsevier.com/locate/jnucmat

Effects of chemical composition and dose on microstructure evolution and hardening of neutron-irradiated reactor pressure vessel steels

T. Takeuchi [a,*], A. Kuramoto [b], J. Kameda [c], T. Toyama [b], Y. Nagai [b], M. Hasegawa [d], T. Ohkubo [c], T. Yoshiie [e], Y. Nishiyama [a], K. Onizawa [a]

[a] *Japan Atomic Energy Agency, Tokai, Ibaraki 319-1195, Japan*
[b] *The Oarai Center, Institute for Materials Research, Tohoku University, Oarai, Ibaraki 311-1313, Japan*
[c] *National Institute for Materials Science, Sengen, Tsukuba 305-0047, Japan*
[d] *Cyclotron and Radioisotope Center, Aoba, Sendai, Miyagi 980-8578, Japan*
[e] *Research Reactor Institute, Kyoto University, Kumatori, Sennan, Osaka 590-0494, Japan*

ARTICLE INFO

Article history:
Received 20 January 2010
Accepted 9 April 2010

ABSTRACT

The correlation of microstructure evolution and hardening was studied in two kinds of A533B-1 steel with high and low levels of Cu irradiated in a range of dose from 0.32 to 9.9×10^{19} n cm^{-2} ($E > 1$ MeV) under a high flux of about 1.7×10^{13} n cm^{-2} s^{-1} using three-dimensional local electrode atom probe (3DAP), positron annihilation (PA) techniques, and Vickers microhardness. The early rapid hardening was found to be caused by mainly matrix defects such as mono- or di-vacancies ($V_1 - V_2$) and/or dislocations indicated by the PA analysis. The 3DAP analysis showed that dense dispersion of dilute Cu rich clusters and lean distribution of Mn–Ni–Si rich clusters, which were identified to possess the same dislocation-pinning effect by applying a Russell and Brown model, were responsible for large and small hardening in high- and low-Cu steels irradiated above 0.59×10^{19} n cm^{2}, respectively.

1. Introduction

Neutron irradiation causes the embrittlement of reactor pressure vessel (RPV) steels of the light water reactors, which is attributed to the formation of solute nano-clusters (SCs), matrix defects (MDs), and their complexes [1–6]. The irradiation-induced microstructural evolution results in hardening of the steel through obstructing the movement of dislocations, thereby causing degradation of the fracture properties, such as the ductile-to-brittle transition temperature shift.

The type and amount of irradiation damage are strongly affected by the metallurgical and irradiation conditions. The formation of SCs have been generally thought to be Cu rich clusters (CRCs) in high-Cu (>0.07 wt.%) steels and to be Mn–Ni(–Si) rich clusters (MNSCs) in low-Cu (<0.07 wt.%) steels [7–9]. Moreover, the retardation of Cu clustering is revealed under neutron higher neutron fluxes [10]. The magnitude of the MDs contribution to hardening has been thought to vary depending on the steel chemical composition, irradiation flux and temperature [6,11–14]. These complicated aspects of irradiated-induced microstructural change make it difficult to understand the mechanisms of hardening and embrittlement of RPV steels.

The SCs can be well characterized by recently developed three-dimensional atom probe (3DAP) tomography. In addition, the statistical accuracy in analyzing SCs is much improved by state-of-art local electrode-type 3DAP techniques that allow to observe the larger volume with a higher rate than a conventional system [15,16]. Vacancy-type defects, vacancy–solute complexes, and dislocations and/or dislocation loops, considered for MDs can be detected by a positron annihilation (PA) technique. Using the PA technique, it is possible to analyze some kinds of defect-free embedded precipitates, such as Cu rich precipitates, in the Fe matrix, which can trap positrons in a "positron quantum dot" state in the irradiated RPV steels. Thus, combining 3DAP and PA is a very useful way to characterize separately the nano-scale formation of both the SCs and MDs.

In this study, we investigated two kinds of high- and low-Cu containing A533B-1 steels neutron-irradiated in a wide range of dose from 0.32 to 9.9×10^{19} n cm^{-2} ($E > 1$ MeV) with an almost constant flux of 1.7×10^{13} n cm^{-2} s^{-1} ($E > 1$ MeV) using a Japan Material Testing Reactor (JMTR). The microstructure changes induced by neutron irradiation were analyzed using laser-assisted 3DAP and PA techniques, and the mechanical property change was analyzed using Vickers microhardness. The effects of the composition and neutron dose on the microstructure evolution are discussed in terms of its correlation with hardening.

---

* Corresponding author.
E-mail address: takeuchi.tomoaki@jaea.go.jp (T. Takeuchi).

0022-3115/$ - see front matter © 2010 Elsevier B.V. All rights reserved.
doi:10.1016/j.jnucmat.2010.04.008

2. Materials and irradiation

The materials studied were the two kinds of low- and high-Cu A533B type steels, designated as Steels A and B, respectively [17,18]. Their chemical compositions are listed in Table 1. The austenitization at 860–893 °C for 7 h and quenching into cold water followed by tempering at 650–660 °C for 6 h. These steels were neutron-irradiated in the JMTR. The use of a pseudo-shroud-type irradiation rig [19] made it possible to produce five different fast neutron doses ($0.32–9.9 \times 10^{19}$ n cm^{-2}) under almost the same flux ($1.6–1.9 \times 10^{13}$ n cm^{-2} s^{-1}) at 290 ± 2 °C. The detailed irradiation conditions are listed in Table 2.

Prior to the irradiation, these steel samples were initially cut into $\varphi 3 \times 0.3$ mm disks and $0.5 \times 0.5 \times 10$ mm needles for PA and 3DAP analyses, respectively. The irradiated disks for the PA analysis were chemically polished in a 5% hydrogen peroxide with 5% hydrofluoric acid and the irradiated needles for 3DAP were first electrochemically polished, first, in an acetic acid solution with a mixture of 25% perchloric acid, and next, in a 2-butoxyethanol with 2% perchloric acid [20]. The polished samples were finally sharpened by a dual-beam FIB/SEM ion milling system [21]. The damage layer due to gallium implantation was diminished by decreasing the incident ion energy in final process of fabrication.

3. Experimental

Vickers microhardness tests were carried out by applying a 200 g load on the surface of needle samples, which had been mounted into epoxy resins and polished mechanically and chemically. The average values of the hardness were obtained from about 30 indentations for each sample.

Positron lifetime measurements were carried out using a digital oscilloscope and three BaF$_2$ scintillators [22] mounted on each photomultiplier tube, i.e., double-stop setup, to reduce high background due to random coincidence with γ-rays from the radiation-induced activities of the specimens than single-stop setup, and a total time resolution of about 170 ps full-width at the half-maximum. The total counts of about 3×10^6 were accumulated for each spectrum.

Coincidence Doppler broadening (CDB) spectra of positron annihilation radiation were obtained by using two Ge semiconductor detectors for coincidence. Because the coincidence measurement realizes a lower background by three orders of magnitude smaller than that of a single detector setup, it is possible to measure the momentum distribution, p_L, in its high-momentum region reflecting that of elementally specific core electrons [23]. The total momentum resolution was about 4×10^{-3} m_0c, where m_0 is the electron/positron rest mass and c is the speed of light. The details of the setup are described in Ref. [23].

The CDB ratio spectra were determined by normalizing the momentum distribution of each spectrum to that of a well-annealed pure Fe. The characteristic broad peak appears in the high-momentum region of around 25×10^{-3} m_0c due to positrons annihilation into Cu 3d electrons. The fraction of low and high-momentum components (LMCF and HMCF) are defined by the count ratio in low momentum ($|p_L| < 4 \times 10^{-3}$ m_0c) and high-momentum (18×10^{-3} $m_0c < |p_L| < 30 \times 10^{-3}$ m_0c) regions in the CDB spectrum with respect to the total counts. The LMCF and HMCF are very sensitive to vacancy-type defects. This is because the positron has much higher probabilities of annihilation with valence electrons spreading out from the surrounding into the open volumes of vacancies. Furthermore, the HMCF strongly reflects the chemical environment of the trapping site of positrons through their annihilation with the core electrons [24], such as vacancy-impurity complexes and CRCs.

The 3DAP analysis of the irradiated steel was carried out with a laser-assisted LEAP by IMAGO Scientific Instruments [16,25] equipped with an energy-compensating reflectron lens [20,26,27]. The laser-assisted LEAP analysis was performed at a laser pulse power of 0.5 nJ, a repetition rate of 200 kHz, and a specimen temperature of 35 K. The high DC bias was typically in a range from 3 to 10 kV. SCs were sorted out from the matrix phase using the maximum separation algorithm based on a friend-of-friends concept [20,28]. The parameters used to identify the SCs were a maximum separation distance, $d_{\max}$, of 0.7 nm and a minimum number of atoms, $N_{\min}$, of 20 atoms. The size of each cluster, i.e., the radius of gyration (l_g), was estimated from the position of the solute atoms in the cluster given by

$$l_g = \sqrt{\frac{\sum_{i=1}^{n}(x_i - x_c)^2 + (y_i - y_c)^2 + (z_i - z_c)^2}{n}}, \quad (1)$$

where x_i, y_i and z_i are the spatial coordinates of each atom, n is the number of atoms in the cluster, and x_c, y_c and z_c are the center of mass. To estimate the composition of SCs in this study, we use the algorithm which considers all atoms within a distance, $L = 0.7$ nm, from any selected solute atom as clustered atoms, and removes all atoms within a distance, $e = 0.5$ nm, from any unselected matrix atom [29,30]. Other methods using the fine voxels (envelope method) [20] or the isoconcentration interface (proxigram) [15,31] have also been generally used to estimate the composition of SCs. The volumes for this analysis were carefully selected by excluding grain boundaries, dislocations and carbides. About a few hundred million atoms were typically collected for each sample.

Table 1
Chemical compositions (wt.%) of the Steel A and Steel B.

	C	Si	Mn	P	S	Ni	Cr	Cu	Mo
Steel A	0.19	0.30	1.30	0.015	0.010	0.68	0.17	0.16	0.53
Steel B	0.19	0.19	1.43	0.004	0.001	0.65	0.13	0.04	0.50

Table 2
Irradiation condition of the Steel A and Steel B.

Reactor	Temperature (°C)	Dose (>1 MeV) ($\times 10^{19}$ n cm^2)	Flux (>1 MeV) ($\times 10^{13}$ n cm^2 s)
JMTR	290 ± 2	0.32	1.8
		0.59	1.6
		1.5	1.6
		3.9	1.8
		9.9	1.9

4. Results

4.1. Vickers microhardness

Figs. 1 and 2 show the relationship of the Vickers microhardness and the amount of irradiation hardening to the dose for both the Steel A and Steel B. For both the unirradiated steels, the hardness remained almost at the same value around 190. Both the high- and low-Cu steel exhibited rapid hardening at low doses below 0.59×10^{19} n cm^{-2} and gradual hardening with further increasing irradiation dose. It is important to point out that the amount of hardening for the irradiated Steel A was larger than that for the Steel B at the early stage of the irradiation. The total hardening for the Steel A irradiated up to 9.9×10^{19} n cm^{-2} is about twice as large as that for the Steel B irradiated to the same dose.

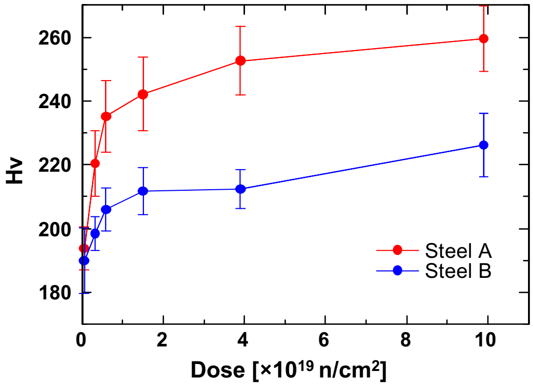

Fig. 1. Variation of Vickers microhardness for the Steel A and Steel B with dose.

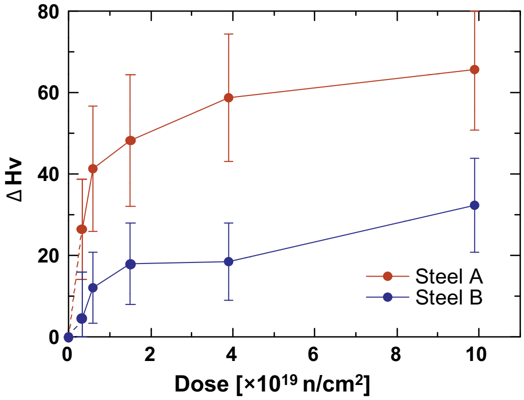

Fig. 2. Variation of irradiation hardening for the Steel A and Steel B with dose.

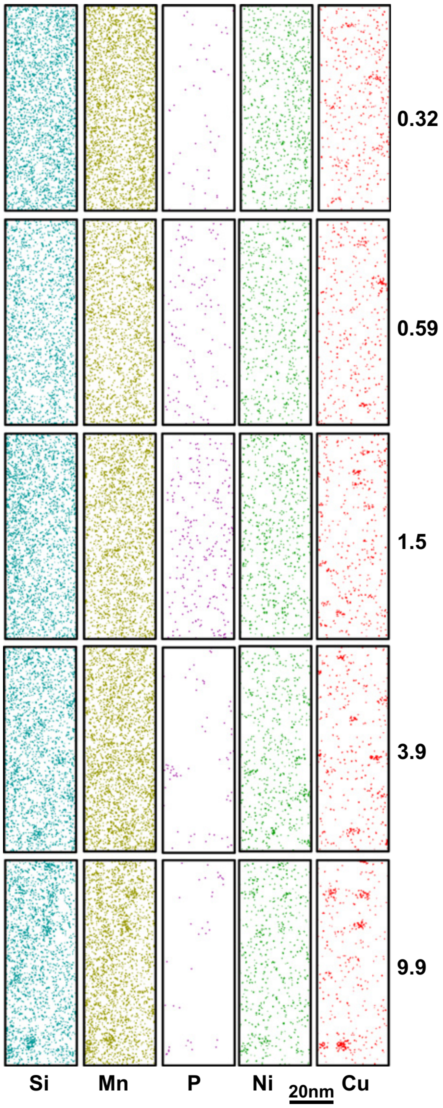

Fig. 3. Atom maps of the solute for the Steel A with dose. Dose is in units of 10^{19} n cm^{-2}.

4.2. LEAP observation

Typical solute atom maps of the Steel A and B subjected to different doses are shown in Figs. 3 and 4. These maps reveal approximately spherical SCs with about 1–2 nm radius (r) in both the steels. These atom maps indicate the formation of Cu-, Mn-, Ni-, Si- and slightly P-enriched clusters, that is CRCs, in the Steel A even irradiated even at the lowest dose and that of Mn-, Ni-, Si- and slightly P-enriched clusters (MNSCs) in the Steel B irradiated to the maximum dose.

The variations of the radius of gyration and the number density (N_d) of the SCs together with the volume fraction V_f (=$4\pi r^3 N_d/3$) for both the steels with dose are shown in Fig. 5. In both the Steel A and Steel B, the radius increased gradually with dose in a similar manner. The number density of SCs also increased with dose in both the steels except for the Steel A irradiated in a dose range from 3.9 to 9.9 × 10^{19} n cm^{-2}. This suggests the coarsening of the CRCs in this dose range in the Steel A.

The average chemical compositions of the SCs in the Steel A and Steel B irradiated at different dose are shown Figs. 6 and 7. The formations of the CRCs in the Steel A and MNSCs in the Steel B are clearly confirmed. In the irradiated Steel B, the concentration of Si in the SCs increased while that of Mn decreased with increasing dose; the sum of Si and Mn concentration is almost constant. In the Steel A irradiated to 9.9 × 10^{19} n cm^{-2}, a increase of the concentration of Si in the SCs occurred by replacing Mn. This is very similar to the change in Si and Mn compositions in the Steel B.

As indicated Fig. 8, the Cu concentration of the Steel A in the matrix phase asymptotically decreased to about 0.05 at.% with increasing dose. This indicates that more Cu atoms are removed from matrix to form the CRCs. However the residual Cu concentration remains at about 0.03 at.% regardless of the dose for the Steel B.

The number of Cu atoms in each cluster is plotted against the total number of Cu, Si, Mn and Ni atoms for the various doses in Fig. 9.This figure indicates how the neutron does affect the number of Cu atoms in each cluster with different sizes. Under 9.9 × 10^{19} n cm^{-2}, the atom number of each clusters with less Cu atoms increases. There is possibility of the presence of some newly nucleated clusters while the high dose is applied. This implies not only the coarsening of the high-Cu SC but also some nucleation of smaller size of low-Cu SCs even in the heavily irradiated high-Cu Steel A. The Steel A irradiated at the dose of 3.9 × 10^{19} n cm^{-2} shows a monomodal distribution of the number of Cu atoms in the CRCs: (a), whereas become to shows a bimodal distribution at the dose of 9.9 × 10^{19} n cm^{-2} (b) in Fig. 10. As the consequence of discussion above, the peak in high-Cu atoms region and low-Cu atoms region probably corresponds to the coarsened high-Cu SCs and the new nucleated low-Cu SCs, respectively.

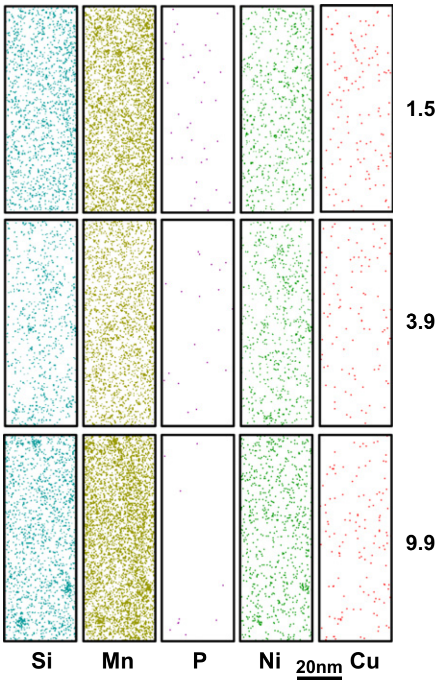

Fig. 4. Atom maps of the solute for the Steel B with dose. Dose is in units of 10^{19} n cm^{-2}.

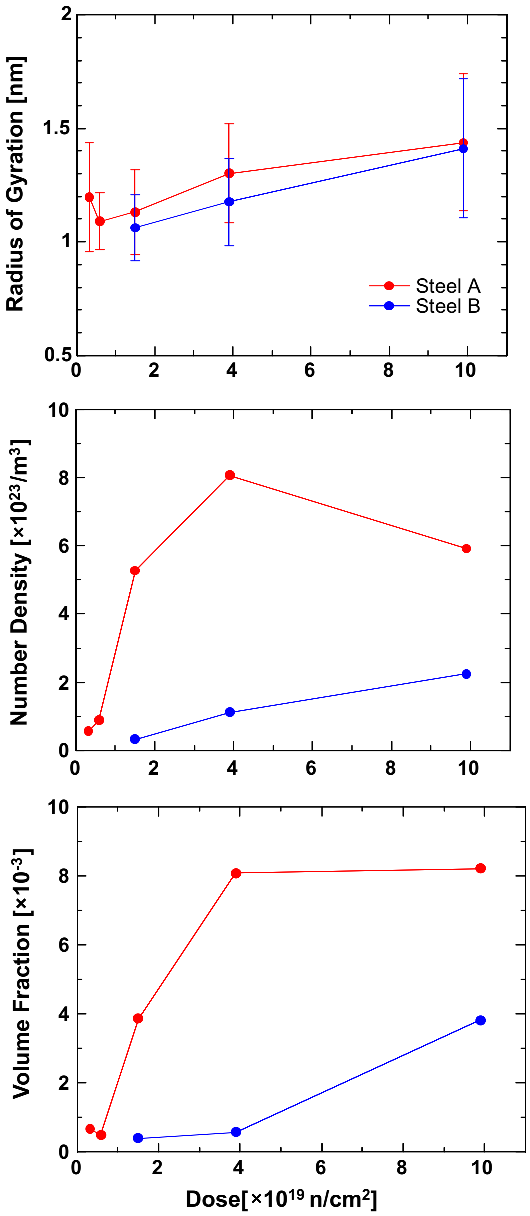

Fig. 5. Variations of the radius of gyration (r), the number density (N_d) and the volume fraction of the SCs for the Steel A and Steel B with dose.

4.3. Positron annihilation

4.3.1. Positron lifetime

All the positron lifetime spectra after the positron source component and background subtraction were well decomposed into two lifetime components. The shorter (τ_1) and longer (τ_2) lifetime components, together with the relative intensities of I_1 and I_2 ($I_1 + I_2 = 1$) are plotted against the dose for the Steel A and Steel B in Fig. 11. The mean positron lifetimes ($\tau_{av} = \tau_1 \times I_1 + \tau_2 \times I_2$) and the theoretical positron lifetime of mono- (V_1) and di-vacancies (V_2) along [1 0 0] direction in Fe matrix are also indicated by dashed lines [32]. Both the unirradiated steels show longer mean positron lifetimes than that for well-annealed pure Fe. This suggests that the positron is trapped at defects introduced during the fabrication of steels.

At the early stage of irradiation up to 0.59×10^{19} n cm^{-2}, the mean positron lifetime for both the steels was rapidly prolonged with the dose, which is due to a large increase in the fraction of positrons trapped at MDs. The longer lifetime component of about 150–200 ps reflects the upper limit of the defect size. These values correspond to the positron lifetime in small size defects, i.e. $V_1 - V_2$, dislocations and/or dislocation loops [33,34]. Thus, almost no larger vacancy clusters or microvoids have formed during irradiation at 290 °C. The values of τ_{av} and τ_2 are very similar in both the irradiated steels and therefore the type and the size of the defects introduced in the Steel A and Steel B in the early stage be almost the same.

In the Steel B irradiated above 0.59×10^{19} n cm^{-2}, both τ_2 and the corresponding intensity I_2, which reflects the number density of small size defects in this case, stay almost constant, thereby suggesting the saturation of the positrons trapped at irradiation-induced defects. In contrast, in the irradiated Steel A, the values of τ_{av} and I_2 decrease with the dose as a result of the increase of positrons trapped to the CRCs (the positron lifetime in the Cu bulk is ~110 ps) [35].

4.3.2. Coincidence Doppler broadening

Figs. 12 and 13 show the CDB ratio curve for the unirradiated and irradiated Steel A and Steel B, respectively. In these figures, the ratio curve of well-annealed pure Cu and pure Fe (8.3×10^{18} n cm^{-2} ($E > 1$ MeV, 100 °C)) are also shown as references. Unfortunately, the ratio curves of the samples irradiated to the highest dose (9.9×10^{19} n cm^{-2}) were unable to be measured because of the high background due to the radioactivity.

In the unirradiated specimens, the enhancement of the ratio curves at the low momentum region reflects the existence of the defects before irradiation as mentioned in the Section 4.3.1. For the unirradiated Steel B, the almost flat curve at the high-momentum region indicates all the positrons annihilate with the electrons of Fe but not CRCs or solute–vacancy complexes. For the unirradiated Steel A, however, the slight peak at around 2.5×10^{-2} m_0c probably arises from imperceptible CRCs or Cu-vacancy complexes introduced during fabrication suggested in Ref. [36].

A broad peak of the ratio spectra was observed as for the pure Cu in the momentum of 25×10^{-3} m_0c in the Steel A irradiated to 0.32×10^{19} n cm^{-2}. This peak increases with the dose, which

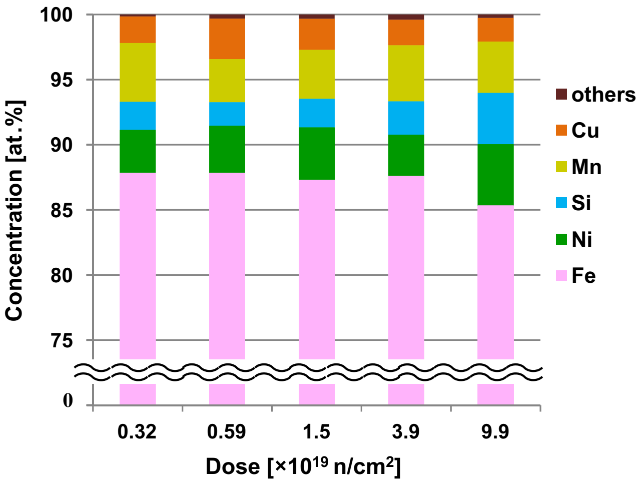

Fig. 6. Average compositions of the solute clusters in the Steel A with dose.

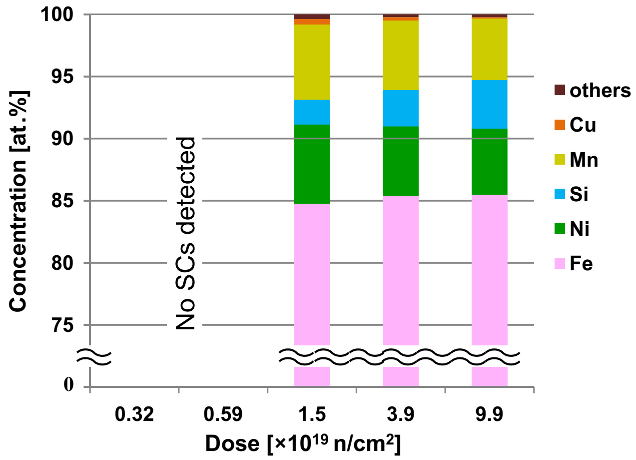

Fig. 7. Average compositions of the solute clusters in the Steel B with dose.

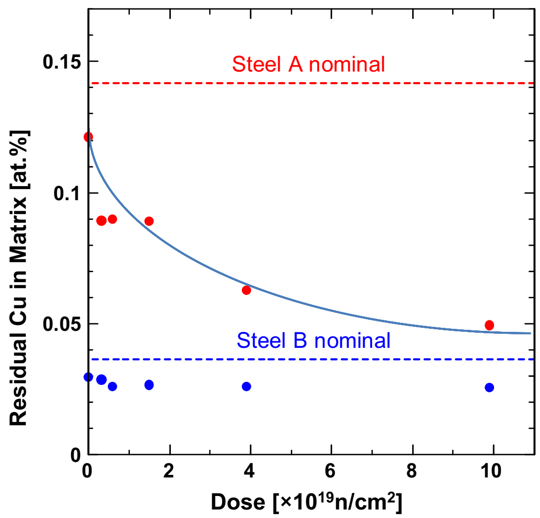

Fig. 8. Variation of residual Cu in matrix in the Steel A and Steel B with dose estimated from 3DAP measurements as a function of the dose. The curve drawn is guide for the eye.

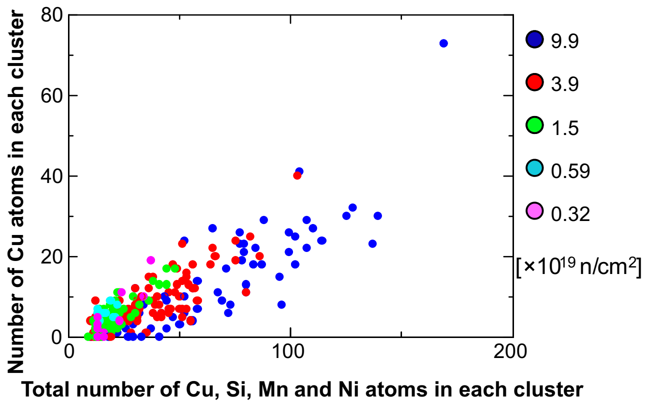

Fig. 9. Number of Cu atoms versus total number of Cu, Si, Mn and Ni in each cluster in Steel A with dose. Note the rising up of the slope from not origin at 9.9×10^{19} n cm^{-2}.

means that the more positrons are trapped in the CRCs and annihilate with the Cu 3d electrons. However no peaks around $25 \times 10^{-3}\ m_0c$ were observed in the Steel B, which suggests no CRCs formation. This difference of the broad peak in the Steel A and B is consistent with the 3DAP observation (Figs. 3 and 4).

The correlation between LMCF and HMCF are plotted in Fig. 14. For the Steel A irradiated with the doses ranging from 0.32 to 0.59×10^{19} n cm^{-2}, the increase with the dose in the LMCF shows the formation of the MDs and the increase in the HMCF shows the formation of the CRCs, or the vacancy-Cu complexes. With the higher dose than 0.59×10^{19} n cm^{-2}, the correlation point shift toward the pure Cu is related to an increase in a fraction of the positrons trapped by the CRCs. In the Steel B, the neutron irradiation caused a shift of the correlation point as observed in irradiated pure Fe. This is due to the absence of CRCs or vacancy-Cu complexes formation and the accumulation of the positron trapped at MDs.

5. Discussion

On the basis of the present PA and 3DAP analyses, we now attempt to describe the mechanism of irradiation hardening observed in the high- and low-Cu steels in terms of the role of the MD $\left(\Delta H_v^{\mathrm{MD}}\right)$ and SC $\left(\Delta H_v^{\mathrm{SC}}\right)$. The total hardening is represented by

$$\Delta H_v^{\mathrm{IRR}} = \Delta H_v^{\mathrm{MD}} + \Delta H_v^{\mathrm{SC}}. \quad (2)$$

A Russell and Brown (RB) model [37] has quantified the motion of dislocation hindered by dispersed obstacles like precipitates and solute clusters, giving rise to obstacle-controlled hardening. In the RB model, the hardening $\left(\Delta\sigma_y^{\mathrm{SC}}\right)$ can be given by

$$\Delta\sigma_y^{\mathrm{SC}} = f_s G_2 (b/L)\{1-(E_1/E_2)^2\}^{3/4}, \quad (3)$$

where

$$\frac{E_1}{E_2} = \frac{G_1}{G_2}\cdot\frac{\log(r/r_0)}{\log(R/r_0)} + \frac{\log(R/r)}{\log(R/r_0)}. \quad (4)$$

In Eqs. (3) and (4), f_s is the Schmid factor, G_1 is the cluster shear modulus, G_2 is the matrix shear modulus, b is the Burgers' vector (=0.248 nm), r_0 is the inner cutoff radius of the dislocation, R is the outer cutoff radius of the dislocation, L is the inter-particle spacing, which is given by $L = 1.77\ r/V_f^{0.5}$.

$(\Delta\sigma_y^{\mathrm{SC}})$ can be converted into $(\Delta H_v^{\mathrm{SC}})$ using $\Delta H_v^{\mathrm{IRR}} = 0.41\Delta\sigma_y^{\mathrm{IRR}}$ reported for low-alloy steels [38] and $f_s = 2.5$ together with Eq. (5).

$$\Delta H_v^{\mathrm{SC}} = 0.58 G_2 (b/r)\{1-(E_1/E_2)^2\}^{0.75} V_f^{0.5}. \quad (5)$$

In order to evaluate the SC hardening, the value of $(\Delta H_v^{\mathrm{SC}})$ was calculated from V_f and r using Eqs. (4) and (5), together with $r_0 = 2.5\ b$, $R = 2500\ b$, $G_2 = 49$ GPa [37], for the steel A and B irradi-

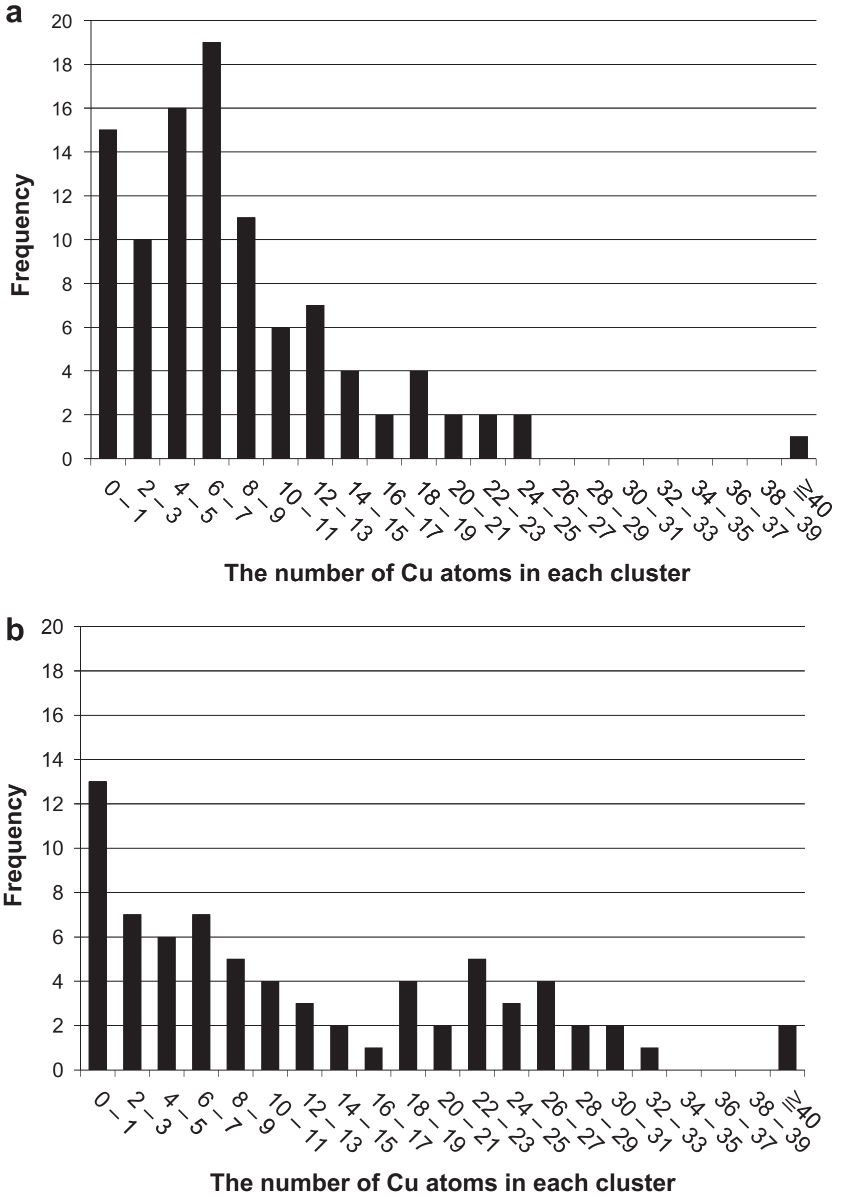

Fig. 10. The histogram of Cu atom numbers in each cluster in the Steel A irradiated to 3.9×10^{19} n cm^{-2} (a) and 9.9×10^{19} n cm^{-2} (b).

ated to more than 0.59×10^{19} n cm^2 (Fig. 15). The shear modulus ratio can be estimated by least-square fitting between the experimentally and theoretically determined (ΔH_v^{SC}) with the slope of 1 representing one to one relation. The estimated G_1/G_2 values of 0.938 and 0.940 for the irradiated steel A and B are reasonable for dilute solute clusters. In Fig. 15, the data are plotted along the x-axis ($\Delta H_v^{SC} = 0$) if no SC are detected by the 3DAP analysis.

The x-intercept of these fitted lines are 30 and 12 for Steel A and B, respectively. Then, the parallel shift along the x-axis from the dashed line is considered to represent the MD hardening (ΔH_v^{MD}).

The several features are pointed out: (i) ΔH_v^{SC} and ΔH_v^{IRR} are linearly correlated with each other except for the result of the Steel A and B samples irradiated to the lowest dose; (ii) it is reasonable to assume that the MD contribution to hardening would diminish by 0.59×10^{19} n cm^{-2} for both the steels in accordance with the results of the PA analysis; (iii) the MD hardening (ΔH_v^{MD}), represented by the parallel shift from the dashed line, can be observed for the irradiated high- and low-Cu steels, and are maximized corresponding to ΔH_v^{MD} of 30 and 12, respectively.

The present 3DAP analysis has shown that under the high irradiation flux in JMTR the hardening is strongly controlled by an increase in the density of dilute solute clusters with weak pinning strength ($G_1/G_2 = 0.94$). It is important to discuss the different characteristics of irradiation damage observed under high irradiation fluxes and in-service irradiation conditions of nuclear reactors. Fukuya and coworkers [39] have reported nanostructural evolution of A533B steel with Cu contents of 0.12 and 0.16 wt.% subjected to irradiation doses from 3.1 to 6.8×10^{19} n cm^{-2} under a wide range of flux from 7.8×10^{10} to 5×10^{12} n cm^{-2} s^{-1}, the former of which is the in-service operation condition. A similar study has been made on surveillance specimens weld metals with the Cu content of 0.13 and 0.3 wt.% by Toyama et al. [40] and on the various specimens irradiated in testing reactors by Soneda et al. [41]. The interesting features are summarized as follows. While the solute content of SCs does not much change with increasing dose (Fig. 6), it changes depending on the irradiation flux. As indicated in Fig. 16, the solute concentration of SCs gradually decreases up to the flux of 5×10^{12} n cm^{-2} s^{-1} and rapidly drops under the irra-

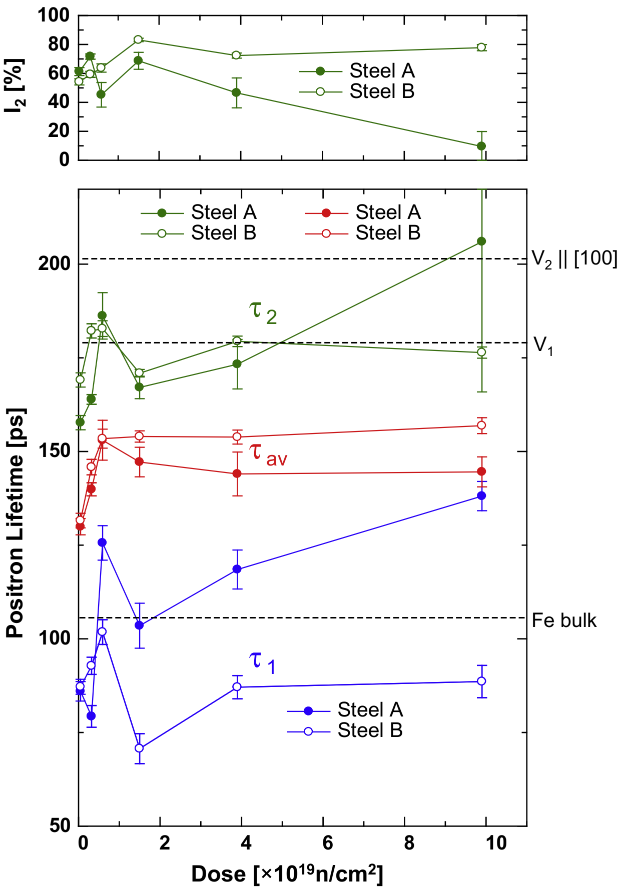

Fig. 11. Relationship of positron lifetime parameters such as short and long life (τ_1 and τ_2), average lifetime (τ_{av}) and relative intensity of short and long lifetime (I_1 and I_2) for the Steel A and Steel B with dose. Calculated positron lifetimes at Fe bulk, the mono- (V_1) and the di-vacancies (V_2) along [1 0 0] direction in Fe matrix are also indicated by dashed lines.

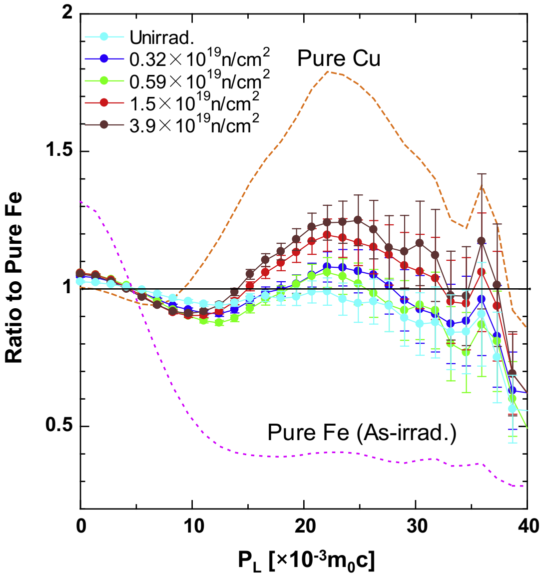

Fig. 12. Ratio curves of the CDB spectra for the unirradiated and irradiated Steel A.

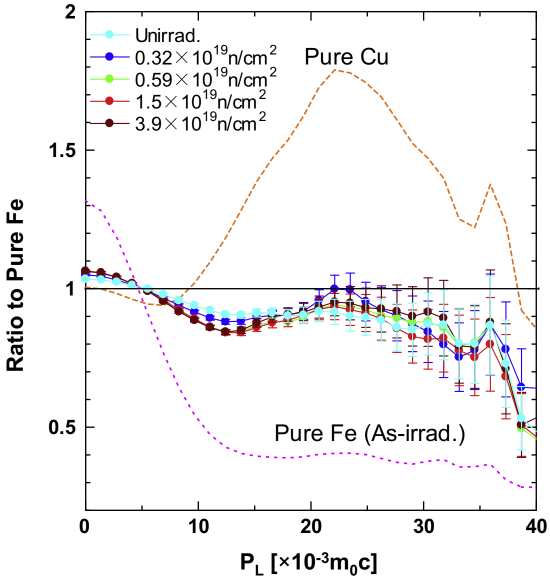

Fig. 13. Ratio curves of the CDB spectra for the unirradiated and irradiated Steel B.

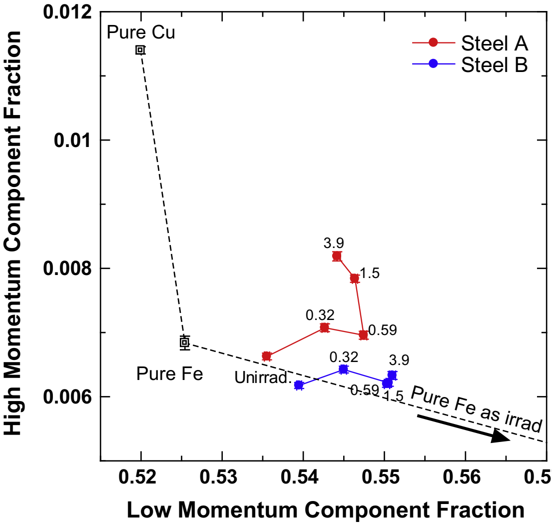

Fig. 14. High/low momentum component fractions of CDB spectra for the irradiated Steel A and Steel B. The values in figure show the dose of neutron irradiation in units of 10^{19} n cm^{-2}. The data for the well-annealed pure Fe, pure Cu, and the neutron-irradiated pure Fe are also plotted as references.

diation flux of 1.7×10^{13} n cm^{-2} s^{-1}. Conversely, the volume fraction is enhanced by increasing the flux. The results for the steel subjected to a dose range from 3.1 to 4.4×10^{19} n cm^{-2} are indicated in Fig. 17. It is possible that such solute rich clusters with low shear modulus that are produced by the low irradiation flux would cause large hardening by the strong pinning effect even if the volume fraction is small. Surveillance samples irradiated below 10^{18} n cm^{-2} have indicated the occurrence of solute clustering, despite the threshold of the criteria in searching the SCs is rather low [42]. Additionally, coarsening and density reductions of CRCs like thermal over ageing behavior can be more readily observed at 10^{19} n cm^{-2} under the surveillance flux condition [40], compared with the present result after 10^{20} n cm^{-2}.

The flux dependence on the composition and density of SCs would be related to the production and annihilation of irradiation-induced defects, which are important factors controlling the solute clustering. Yet, it is difficult to examine the nucleation and growth mechanisms of SCs in terms of the dynamic interaction of solute with irradiation-induced defects. Bases on the differing

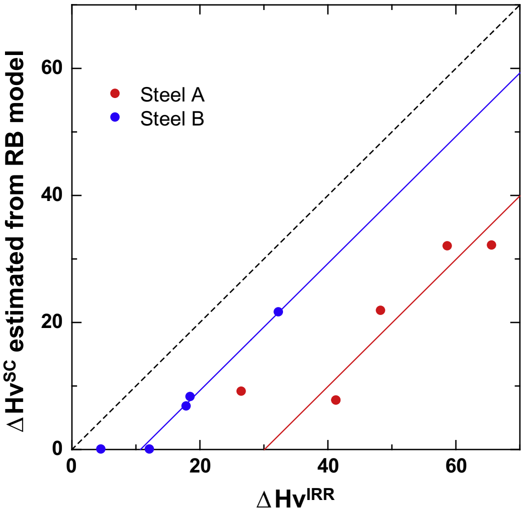

Fig. 15. Comparison of the measured irradiation hardening with that estimated from Russell and Brown model. The results with G_1/G_2 at 0.938 and 0.940 for Steel A and B are shown, respectively. The lines drawn are least-squares fitted to the data in the steel irradiated to more than 0.59×10^{19} n cm^{-2}.

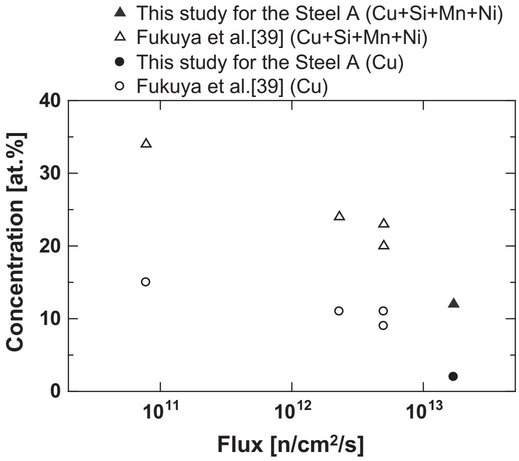

Fig. 16. Flux dependence of solute concentration of SCs in the alloys with the Cu content of 0.12–0.16 wt.%.

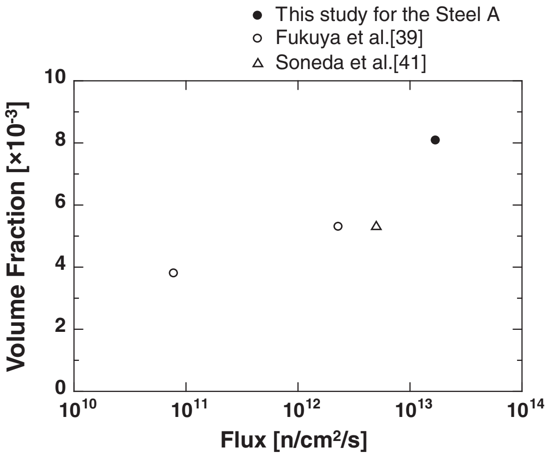

Fig. 17. Flux dependence of volume fraction of SCs in the alloys with the Cu content of 0.12–0.17 wt.% subjected to a dose range from 3.1 to 4.4×10^{19} n cm^{-2}.

nanostructural evolution under the high and low fluxes, it is speculated that as the irradiation flux is increased, the density of SCs nucleation sites that is the aggregation of vacancies would be enhanced and therefore the SCs would be composed of dilute solute probably due to the large partitioning of solute among a number of clusters. On the contrary, decreasing the flux would lower the number of vacancy aggregation sites, giving rise to the formation of solute-concentrated clusters. Consequently, discrete clustering dominates hardening during the low flux associated with negligible matrix damage controlling hardening.

It is found that the formation of low-Cu SCs similar to MNSCs can occur even in the Steel A subjected to the maximum dose. This phenomenon probably corresponds to “late blooming” phase [14], which is thought to arise only in the low-Cu steel and rapidly grow up with dose. At the maximum dose, the chemical environment seems to be similar to that of the Steel B since the Cu concentration dissolved in the matrix phase is close to the nominal level of the Steel B. Therefore, it is necessary to take into account the possibility of rapid embrittlement even after the saturation of the CRC clustering in the high-Cu steel.

6. Summary and conclusions

This study reports the effects of the composition and dose on microstructure evolution and hardening in high-Cu and low-Cu A533B-1 steels neutron-irradiated in a wide range from 0.32 to 9.9×10^{19} n cm^{-2} under a constant high flux of about 1.7×10^{13} n cm^{-2} s^{-1}. The Vickers microhardness tests showed the rapid hardening for both the steels irradiated up to 0.59×10^{19} n cm^{-2} followed by gradual hardening with increasing irradiation dose. The high-Cu steel exhibited larger irradiation hardening than the low-Cu steel. The PA and 3DAP techniques clearly demonstrated supporting results of more substantial microstructure evolution in the high-Cu steel. At the early stage of irradiation, small size defects such as $V_1 - V_2$ or dislocations are rapidly induced in the high- and low-Cu steels. The CRCs formed even at 0.32×10^{19} n cm^{-2} and start coarsening at around 3.9×10^{19} n cm^{-2} in the high-Cu steel, while the MNSC formation was retarded till $\sim 1 \times 10^{19}$ n cm^{-2} and still grow at around 1×10^{20} n cm^{-2} in the low-Cu steel. Moreover, the formation of low-Cu SCs similar to MNSCs is suggested at the highest dose in the high-Cu steel. This phase can cause the additional embrittlement at the very high dose.

By applying a RB model, it was found that the dislocation-pinning strength of the CRCs and MNSCs is the same and the magnitude of MD and SC controlling the rapid hardening at the early stage of irradiation and the gradual hardening from the middle to the later stage of irradiation, respectively, are characterized in the two types of steel. The different characteristics of solute clustering induced during the high irradiation flux and very low flux operated in-service nuclear reactor are discussed in light of the nucleation process.

Acknowledgements

This study was partially supported by Grant-in-Aid for Specially Promoted Research (17702009) and for Scientific Research (A) (21246142) of the Ministry of Education, Culture, Sports, Science and Technology (MEXT), and by the Budget for Nuclear Research of the Ministry of Education, Culture, Sports, Science and Technology, based on the screening and counseling by the Atomic Energy Commission, and was carried out under the Cooperative Research Program of International Research Center for Nuclear Materials Science, Institute for Materials Research (IMR), Tohoku University.

The authors would like to thank M. Narui and M. Yamazaki at the Oarai Center for their support for hot laboratory work.

References

[1] G.R. Odette, Scr. Metall. 17 (1983) 1183.
[2] G.M. Worrall, J.T. Buswell, C.A. English, M.G. Hetherington, G.D.W. Smith, J. Nucl. Mater. 148 (1987) 107.
[3] S.B. Fisher, J.E. Harbottle, N. Aldridge, Phil. Trans. R. Soc. Lond. A 315 (1985) 301.
[4] E. Mader, G.E. Lucas, G.R. Odette, Symp. Eff. Radiat. Mater., ASTM STP 1125 (1992) 151.
[5] G.R. Odette, Mat. Res. Soc. Symp. Proc. 373 (1995) 137.
[6] G.R. Odette, G.E. Lucas, Radiat. Eff. Defects Solids 144 (1998) 189.
[7] ASTM E900-02, Standard Guide for Predicting Radiation-Induced Transition Temperature Shift for Reactor Vessel Materials, Annual Book of ATSM Standards, vol. 12.02 (West Conshohocken, PA: American Society for Testing and Materials).
[8] G.R. Odette, W.D. Wirth, J. Nucl. Mater. 251 (1997) 157.
[9] M.K. Miller, A.A. Chernobaeva, Y.I. Shtrombakh, K.F. Russell, R.K. Nanstad, D.Y. Erak, O.O. Zabusov, J. Nucl. Mater. 385 (2009) 615.
[10] Y. Nagai, T. Toyama, Y. Nishiyama, M. Suzuki, Z. Tang, M. Hasegawa, Appl. Phys. Lett. 87 (2005) 261920.
[11] Y. Nagai, K. Takadate, Z. Tang, H. Ohkubo, H. Takizawa, M. Hasegawa, Phys. Rev. B 67 (2003) 224202.
[12] G.R. Odette, T. Yamamoto, D. Klingensmith, Phil. Mag. 85 (2005) 779.
[13] G.R. Odette, JOM 53 (7) (2001) 18.
[14] G.R. Odette, JOM 61 (7) (2009) 17.
[15] M.K. Miller, R.G. Forbes, Mater. Char. 60 (2009) 461.
[16] G.L. Kellogg, T.T. Tsong, J. Appl. Phys. 51 (1980) 1184.
[17] K. Onizawa, T. Tobita, M. Suzuki, JAERI-M 97-081, Japan Atomic Energy Research Institute, November 1997.
[18] K. Onizawa, T. Tobita, M. Suzuki, Symp. Eff. Radiat. Mater., ASTM STP 1366 (2000) 204.
[19] M. Narui, T. Sagawa, T. Shikama, J. Nucl. Mater. 258–263 (1998) 372.
[20] M.K. Miller, Atom Probe Tomography, Kluwer Academic/Plenum Publishing, New York, NY, 2000.
[21] D.J. Larson, D.T. Foord, A.K. Petford-Long, H. Liew, M.G. Blamire, A. Cerezo, G.D.W. Smith, Ultramicroscopy 79 (1999) 287.
[22] H. Saito, Y. Nagashima, T. Kurihara, T. Hyodo, Instr. Meth. Phys. Res. Sect. A 487 (2002) 612.
[23] Y. Nagai, M. Hasegawa, Z. Tang, A. Hempel, K. Yubuta, T. Shimamura, Y. Kawazoe, A. Kawai, F. Kano, Phys. Rev. B 61 (2000) 6574.
[24] Z. Tang, M. Hasegawa, Y. Nagai, M. Satio, Y. Kawazoe, Phys. Rev. B 65 (2002) 045108.
[25] T. Kelly, D. Larson, Mater. Charact. 44 (2000) 59.
[26] W. Drachsel, L.V. Alvensleben, A.J. Melmed, J. de Phys. 50-C8 (1989) 541.
[27] S.J. Sijbrandij, A. Cerezo, T.J. Godfrey, G.D.W. Smith, App. Surf. Sci. 94 (/95) (1996) 428.
[28] J.M. Hyde, C.A. English, Mat. Res. Soc. Symp. 650 (2001) R661.
[29] D. Vaumousse, A. Cerezo, P.J. Warren, Ultramicroscopy 95 (2003) 215.
[30] A. Morley, G. Sha1, S. Hirosawa, A. Cerezo, G.D.W. Smith, Ultramicroscopy 109 (2009) 535.
[31] O.C. Hellman, J.A. Vandenbroucke, J. Rusing, D. Isheim, D.N. Seidman, Microsc. Microanal. 6 (2000) 437.
[32] H. Ohkubo, Z. Tang, Y. Nagai, M. Hasegawa, T. Tawara, M. Kiritani, Mat. Sci. Eng. A. 350 (2003) 95.
[33] Y. Kamimura, T. Tsutsumi, E. Kuramoto, Phys. Rev. B 52 (1995) 879.
[34] M.J. Puska, R. Nieminen, J. Phys. F 12 (1982) L 211. F 13 (1983) 333.
[35] A. Seeger, F. Banhart, Phys. Status Solidi a 102 (1987) 171.
[36] J.M. Hyde, M.G. Burke, R.M. Boothby, C.A. English, Ultramicroscopy 109 (2009) 510.
[37] K.C. Russell, L.M. Brown, Acta Metall. 20 (1972) 969.
[38] J.T. Buswell, W.J. Phythian, R.J. McElroy, S. Dumbill, P.H.N. Ray, J. Mace, R.N. Sinclair, J. Nucl. Mater. 225 (1995) 196.
[39] K. Fukuya, K. Ohno, H. Nakata, S. Dumbill, J.M. Hyde, J. Nucl. Mater. 312 (2003) 163.
[40] T. Toyama, Y. Nagai, Z. Tang, M. Hasegawa, A. Almazouzi, E. van Walle, R. Gerard, Acta Mater. 55 (2007) 6852.
[41] N. Soneda, K. Dohi, K. Nishida, A. Nomoto, M. Tomimatsu, H. Matsuzawa, J. ASTM. Int. 6 (8) (2009) JAI102128.
[42] N. Soneda, K. Dohi, A. Nomoto, K. Nishida, S. Ishino, CRIEPI Report Q06019, 2007 (in Japanese).